

This is a repository copy of *Grain-scale dependency of metamorphic reaction on crystal plastic strain*.

White Rose Research Online URL for this paper: http://eprints.whiterose.ac.uk/152120/

Version: Accepted Version

Article:

Chapman, T, Clarke, GL, Piazolo, S orcid.org/0000-0001-7723-8170 et al. (2 more authors) (2019) Grain-scale dependency of metamorphic reaction on crystal plastic strain. Journal of Metamorphic Geology, 37 (7). pp. 1021-1036. ISSN 0263-4929

https://doi.org/10.1111/jmg.12473

© 2019 John Wiley & Sons Ltd. This is the peer reviewed version of the following article: Chapman, T, Clarke, GL, Piazolo, S, Robbins, VA, Trimby, PW. Grain-scale dependency of metamorphic reaction on crystal plastic strain. J Metamorph Geol. 2019; 37: 1021–1036, which has been published in final form at https://doi.org/10.1111/jmg.12473. This article may be used for non-commercial purposes in accordance with Wiley Terms and Conditions for Use of Self-Archived Versions.

Reuse

Items deposited in White Rose Research Online are protected by copyright, with all rights reserved unless indicated otherwise. They may be downloaded and/or printed for private study, or other acts as permitted by national copyright laws. The publisher or other rights holders may allow further reproduction and re-use of the full text version. This is indicated by the licence information on the White Rose Research Online record for the item.

Takedown

If you consider content in White Rose Research Online to be in breach of UK law, please notify us by emailing eprints@whiterose.ac.uk including the URL of the record and the reason for the withdrawal request.





Grain-scale dependency of metamorphic reaction on crystal plastic strain

Journal:	Journal of Metamorphic Geology
Manuscript ID	JMG-18-0068
Manuscript Type:	Original Article
Date Submitted by the Author:	13-Aug-2018
Complete List of Authors:	Chapman, Timothy; The University of Sydney, School of Geosciences Clarke, Geoffrey; University of Sydney, School of Geosciences Piazolo, Sandra; Macquarie University, Department of Earth and Planetary Sciences Robbins, Victoria; The University of Sydney, School of Geosciences Trimby, Patrick; The University of Sydney, Australian Centre for Microscopy and Microanalysis
Keywords:	element diffusion, recrystallization, metamorphic equilibration, microstructures, crystal deformation



1	Grain-scale dependency of metamorphic reaction on crystal plastic strain
2	
3	Timothy Chapman ¹ *, Geoffrey L. Clarke ¹ , Sandra Piazolo ²⁺ , Victoria A. Robbins ¹ and
4	Patrick W. Trimby ^{3^} .
5	
6	¹ School of Geosciences, University of Sydney, NSW, 2006, Australia
7	² ARC Centre of Excellence for Core to Crust Fluid Systems and GEMOC, Department of
8	Earth and Planetary Sciences, Macquarie University, NSW, 2109, Australia
9	³ Australian Centre for Microscopy & Microanalysis, University of Sydney, NSW, 2006,
10	Australia
11	Current address: ⁺ School of Earth and Environment, University of Leeds, United Kingdom;
12	^Oxford Instruments, Oxford, United Kingdom
13	*Corresponding author: <u>t.chapman@sydney.edu.au</u>
14	
15	SHORT TITLE: Grain-scale dependency of reaction on strain
16	
17	ABSTRACT
18	The Breaksea Orthogneiss in Fiordland, New Zealand preserves water-poor intermediate and
19	mafic igneous rocks that were partially recrystallized to omphacite granulite and eclogite,
20	respectively at $P \approx 1.8$ GPa and $T \approx 850$ °C. Metamorphic reaction consumed plagioclase and
21	produced grossular-rich garnet, jadeite-rich omphacite, clinozoisite and kyanite. The extent of
22	metamorphic reaction, identified by major and trace element composition and microstructural
23	features, is patchy on the grain and outcrop scale. Domains of re-equilibration coincide with
24	areas that exhibit higher strain suggesting a causal link between crystal plastic strain and
25	metamorphic reaction. Quantitative orientation analysis (EBSD) identifies gradual and

26	stepped changes in crystal lattice orientations of igneous phenocrysts that are surrounded by
27	homophase areas of neoblasts, characterized by high grain boundary to volume ratios and
28	little to no internal lattice distortion. The limited, peripheral chemical modification of less
29	deformed garnet and omphacite phenod al grains reflects limited lattice diffusion in areas
30	that lacked 3D networks of interconnected low-angle boundaries. Low-angle boundaries
31	appear to have acted as elemental pathways (pipe diffusion) that enhanced in-grain element
32	diffusion. The scale of pipe diffusion is pronounced in garnet relatively to clinopyroxene.
33	Strain-induced mineral transformation largely controlled the extent of high-T metamorphic
34	reaction under relatively fluid-poor conditions.
35	
36	KEYWORDS: element diffusion; recrystallisation; metamorphic equilibration; crystal
37	plastic strain; deformation; microstructures
38	
20	

39 INTRODUCTION

40 Deformation is generally thought to assist metamorphism overcoming kinetic impediments 41 and achieve reaction progress, based on both experimental and field observation (e.g. Brodie 42 & Rutter, 1985; Austrheim, 1987; Rutter & Brodie, 1995). However, the nature of causal 43 grain-scale mechanisms remains largely unconstrained in regional metamorphic terranes that experienced high-grade conditions. Microstructures in granulite facies rocks commonly 44 involve ehen hy homogeneous min of low-energy grain form that lack obvious 45 46 reaction relationships (Powell, Guiraud & White, 2005; Vernon, Collins & Cook, 2012). 47 Such features are assumed to reflect a point of thermodynamic equilibrium whereby rates of 48 intra-crystalline diffusion approached rates of grain boundary diffusion, enabling equilibrium 49 to be maintained on a scale larger than that of the grain (e.g. Marmo, Clarke & Powell, 2002; 50 Powell et al., 2005). Persistent high temperature conditions are also conducive to the

deformation of many common rock-forming minerals plastically via mechanisms such as
dislocation creep (Bürgmann & Dresen, 2008).

53 Microstructures indicative of incomplete reaction and strain localization can be 54 common in exceptionally dry rocks and/or the products of short-lived tectonic events (e.g. 55 Williams & Jercinovic, 2012). Sites that record partial metamorphism enable the 56 identification of kinetic limitations to reaction progress and present phenomena that can be 57 queried to assess the link between crystal plastic strain and metamorphic reaction. Related 58 processes that contribute to reactions overcoming kinetic barriers, such as fluid ingress and/or 59 mechanical reductions in grain size, can result in a decrease in the time- and length-scale of 60 grain-boundary diffusion (Austrheim, 1987; Yund & Tullis, 1991). More pervasive feedback 61 mechanisms can potentially involve the direct coupling of intra-crystalline element mobility, 62 dislocation movement and the production of strain-induced lattice defects. The latter may be 63 difficult to verify in geological samples on account of the time scales involved, which are 64 amenable to physical recovery and secondary ehemical change (Urai, Means & Lister, 1986; 65 Powell et al., 2005). However, a number of reported observations present a compelling link 66 between the production and migration of low- and high-angle boundaries and the formation 67 of new chemically-distinct (equilibrated) grains (e.g. Brodie & Rutter, 1985; Stünitz, 1998; 68 Svahnberg and Piazolo, 2010; Williams & Jercinovic, 2012; Satsukawa et al. 2015). 69 The generation, movement and annihilation of dislocations during crystal plastic 70 deformation can also enhance intra-grain element diffusion (Cottrell, 1953; Ruoff & Ballufi, 71 1963). This may take the form of a sweeping motion of high solute concentrations adjacent to 72 dislocations, as has been observed in zircon (Piazolo et al., 2016). In conjunction with 73 comparatively rapid "pipe" diffusion — the process of diffusing elements along dislocation cores (low-angle boundaries) — pronounced chemica 74 75 volumes of strained lattice (Hart, 1957; Love, 1964). Whereas solid state change through pipe

76	diffusion has been detected in metals (e.g. Legros, Dehm, Arzt & Balk, 2008), the
77	interpretation of equivalent change in silicates has been largely restricted to accessory
78	minerals (Lund, Piazolo & Harley, 2006; Reddy et al., 2006; Piazolo, Austrheim &
79	Whitehouse, 2012). However, based on work we present her concurrence and efficiency
80	of such diffusion in silicates is fundamental to models of ionic diffusion and scale of
81	equilibration (Lasaga, 1979; Marmo et al., 2002; Powell et al., 2005; Ague & Carson, 2013).
82	An iss texplored here is the potential of non-hydrostatic stress to additional influence
83	the nature of chemical equilibrium (e.g. Wheeler, 2014; Powell, Evans, Green & White,
84	2017). We present a quantitative analysis assessing the spatial correlation between chemical
85	modification and the dependency on the presence of deformation induced low-angle
86	boundary networks, gradual lattice distortion and high-angle boundaries in a natural example
87	of lower crustal rocks from New Zealand (Clarke, Daczko & Miescher, 2013; Chapman,
88	Clarke, Piazolo & Daczko, 2017). Low angle boundary networks are shown to provide
89	channel ways of accelerated intra-grain diffusion in garnet and pyroxene during
90	metamorphism compared with the relative restricted length scales recorded along high-angle
91	boundaries in relics of formerly homogeneous igneous phenocrysts. The results from our
92	case-study highlight the fundamental role crystal plastic deformation plays in enhancing
93	metamorphic re-equilibration during solid-state reaction in rock-forming mineral
94	

95 THE BREAKSEA ORTHOGNEISS

96 The *c*. 124–110 Ma Breaksea Orthogneiss is exposed in Breaksea Sound (Fig. 1) and
97 immediate north thereof (Allibone et al., 2009; De Paoli, Clarke, Klepeis, Allibone &
98 Turnbull, 2009; Milan, Daczko, Clarke & Allibone, 2016; Stowell et al., 2017). It is the
99 highest-grade part of the Western Fiordland Orthogneiss, a suite of intermediate to mafic
100 plutons emplaced during an early Cretaceous arc flare-up event (Bradshaw, 1989; Allibone et

101	al., 2009; Chapman, Clarke & Daczko, 2016; Milan, Daczko & Clarke, 2017). The Breaksea
102	Orthogneiss comprises rmediate and mafic layers, thought to have been emplaced into
103	thickened arc crust (De Paoli et al., 2009). Monzodioritic layers are patcher metamorphosed
104	to garnet-omphacite granulite (65%) or omphacite-orthopyroxene granulite (5%) with
105	decametre layers and pods of peridotgab
106	clinopyroxenite, harzburgite and hornblende peridotite (collectively 5%: De Paoli et al.,
107	2009; Clarke et al., 2013; Chapman, Clarke, Daczko, Piazolo & Rajkumar, 2015).
108	Metamorphic assemblages in both intermediate and mafic protoliths reflect c. 1.8 GPa and
109	850°C (De Paoli et al., 2009, De Paoli, Clarke & Daczko, 2012; Clarke et al., 2013; Chapman
110	et al., 2017).
111	Distinctions in the proportions of garnet, clinopyroxene, plagioclase and
112	orthopyroxene throughout the Breaksea Orthogneiss are primarily attributed to cumulate
113	processes and magma redox conditions that preceded high-grade deformation (De Paoli et al.,
114	2009; Chapman et al., 2015). Interlayered near-monomineralic garnetite and clinopyroxenite
115	retain igneous microstructures and mineral chemistry (Clarke et al., 2013). Garnet in eclogite
116	layers is interpreted as igneous on the basis of its major and rare earth element (REE) content
117	being similar through the spectrum of ultrabasic-intermediate compositions, and it-lacking a
118	positive Eu anomaly (Clarke et al., 2013). As garnet and of acite collectively form 90% of
119	eclogite, omphacite in the eclogite layers is also interpreted to be of cumulus origin (Clarke et
120	al., 2013). Despite having an intense, shallowly dipping gneissic foliation, the orthogneiss
121	preserves compositional layering in all rock types (De Paoli et al., 2009; Betka & Klepeis,
122	2013; Chapman et al., 2015; Klepeis, Schwartz, Stowell & Tulloch, 2016). This layering is
123	inferred to be mainly an igneous feature, presumably cumulate, and was transposed into S_1 .
124	In low strain zones, monzodioritic gneiss preserves igneous microstructures consistent with
125	the parental magma having crystallised Ca-Na clinopyroxene with or without garnet or

126	orthopyroxene (Clarke et al., 2013; Chapman et al., 2015). Metamorphic assemblages of
127	omphacite, garnet, plagioclase, kyanite and rutile that define S_1 in monzodioritic gneiss are
128	consistent with metamorphic equilibration at the omphacite granulite sub-facies (De Paoli et
129	al., 2012; Chapman et al., 2017). A series of late magmatic garnet-monzonite veins cross-cut
130	S_1 (Clarke et al., 2013). The whole-rock major and trace element compositions throughout the
131	strained monzodioritic (now granulite) components of the orthogneiss are remarkably
132	consistent, defining a restricted range in silica and total alkali content (SiO ₂ = 50–55 wt %O
133	and $(Na_2O+K_2O) = 5-7$ wt %O: Clarke et al., 2013; Chapman et al., 2015).
134	Igneous and metamorphic paragenesis have been distinguished using a combination
135	of mineral chemistry and microstructural relationships, the overall extent of relict mineralogy
136	varying with strain intensity (Clarke et al., 2013; Chapman, Clarke, Piazolo & Daczko,
137	submitted). Igneous garnet defines large granoblastic garnet grains in clusters with omphacite
138	(Fig. 2a), that retain heavy-REE-enriched patterns overlapping with igneous garnet in
139	eclogite and garnetite (Clarke et al., 2013). In contrast, metamorphic garnet form small
140	idioblastic grains in necklace-style structures between omphacite and plagioclase (Fig. 2b),
141	are heavy-REE depleted and have positive Eu anomalies consistent with metamorphic growth
142	(Clarke et al., 2013). Similarly, igneous clinopyroxene form large calcic grains in clusters
143	with igneous garnet, retaining pronounced lattice distortion and fine exsolution lamellae (Fig.
144	2f). These contrast with small neoblastic grains that are free of substructure and are richer in
145	sodium (Fig. 2). The distinct microstructural form of the relict and neoblastic phases
146	corresponds with differing crystallographic orientations (Chapman et al., submitted).
147	Omphacite neoblasts have orientations consistent with their formation during rotational
148	recrystallization from the larger porphyroclasts. The S_1 grain form present cleation sites
149	for the subsequent epitaxial growth of metamorphic garnet (Chapman et al., submitted).
150	Concurrently, the surrounding feldspar-quartz-rich matrix was extensively recrystallized and

151 chemically modified (Fig. 2). Across differing strain domains in the orthogneiss these

- 152 distinctions in microstructural extent of relict and neoblastic phases has been quantified on a
- 153 thin-section scale (Chapman et al., submitted).

The finer s extent of intra-grain chemical modification in deformed 154 155 porphyroclasts of the Breaksea Orthogneiss has not been assessed. The recovery of 156 petrogenetic information, either through traditional thermobarometic methods or by analysing 157 mineral reaction textures through the pseudosection approach, are dependent on appropriate microstructural interpretations at these scales.g. Powell & Holland, 2008; Vernon, White 158 159 & Clarke, 2008). Establishing the link between thermodynamically controlled mineral 160 chemistry and deformation-induced crystal plastic microstructure in common rock-forming 161 minerals is therefore fundamental to understanding the tectonometamorphic and rheology of 162 the lithosphere. This paper specifically assesses the link between crystal plastic strain and in-163 grain chemical zoning from garnet and pyroxene phenocrysts from the dioritic component of the Breaksea Orthogneiss 164

165

166 **METHODS**

167 Petrographic and microstructural observations were coupled with quantitative

168 crystallographic orientation mapping. All thin sections were prepared perpendicular to the

169 foliation (XY plane) and parallel to the lineation (X direction). Representative examples were

- 170 analysed at high-resolution using the electron back-scatter diffraction (EBSD) technique (e.g.
- 171 Prior et al. 1999). Mineral chemical analysis was undertaken by the scale of EBSD
- 172 mapping to correlate to features of recrystallisation and crystal plastic deformation.

173

174 Quantitative crystallographic orientation analysis

Page 8 of 61

175	Electron back-scatter diffraction (EBSD) investigation was performed using a Zeiss Ultra
176	Plus SEM at the Australian Centre for Microscopy and Microanalysis at the University of
177	Sydney. Etched polished thin sections (~30 μ m) were analysed at an accelerating voltage of
178	20 kV, with a beam current of 8 nA and a working distance of \sim 9–14 mm. Electron
179	backscatter diffraction patterns were automatically acquired and indexed using Oxford
180	Instruments AzTEC software (<u>https://www.oxford-instruments.com/</u>). The EBSD patterns
181	were collected in regular grids where the sampling step size varied from 1–3 μ m for grain-
182	scale analysis and $0.3-0.5 \ \mu m$ for detailed sections of the crystals. Post-processing was
183	undertaken in the HKL Channel 5 TANGO software (Oxford Instruments) following
184	procedures that are designed to remove false data and to enhance data continuity over the
185	microstructures as described by Prior, Wheeler, Peruzzo, Spiess & Storey (2002). In the
186	following analysis, grains are defined as areas enclosed by boundaries of greater than 10° of
187	misorientation; boundaries with misorientations less than 10° but greater than 1° are referred
188	to as low-angle boundaries. The extent of crystal lattice strain in a defined grain area was
189	determined by the average distribution of misorientation, inclusive of the low-angle
190	boundaries in Channel 5.

191

192 Mineral Chemistry

193 *Major elements*

194 Quantitative chemical X-ray maps of crystalline minerals were obtained using the Cameca

195 SX100 electron microprobe housed at the Electron Microscopy and X-ray Microanalysis

196 facility at the University of Tasmania, Hobart. Additional data was also collected on the

197 Cameca SX100 electron microprobe housed at the Research School of Earth Sciences,

198 Australian National University, Canberra. Operating conditions for the analysis involved a

199 15 kV accelerating voltage, 40 nA beam current and 2 µm beam-diameter with dwell times of

300 milliseconds per point. The analyses at the University of Tasmania were collected on five
wavelength-dispersive spectrometers (WDS) using TAP, LPET, PET and LLIF crystals. The
raw data-was processed using the in house '*Probe for EMPA* (Probe Software Inc. Eugene,
USA)' and using the Phi-Rho-Z matrix correction method of Love & Scott (1978). X-ray
intensities were converted to maps of oxide weight percent using the algorithm of Clarke,
Daczko & Nockolds (2001) and visualized following data manipulation procedures described
in Marmo et al. (2002).

208 Trace elements

209 The distribution of trace elements in relation to lattice defects and low-angle boundaries cannot be robustly resolved with point source data broad perspective is obtainable by 210 211 comparing grain regions with lattice distortion and low-angle boundaries to those that lack 212 appreciable substructure. The trace element concentrations of garnet and omphacite were 213 determine though *in-situ* analysis using an Agilent 7700cs quadrupole Inductively Coupled 214 Plasma Mass Spectrometer (ICPMS), attached to a New Wave UP-213 Nd:YAG laser 215 ablation microprobe (LAM) housed at Macquarie Geoanalytical, Macquarie University, 216 Sydney. Data acquisition parameters involved a c. 60 second background count prior to laser 217 ablation and a c. 100–120 second signal analysis period. Operating conditions involved a 218 55 μ m beam diameter and a 5 Hz pulse repetition that produced ~40 μ m deep flat bottom pits. 219 Calcium content determined by the electron microprobe was used to calibrate trace element 220 spectra. The analysis of NIST 610 glass during each session provided an external standard, 221 with individual analysis required to fall within error of long-term laboratory compilations. 222 The internal standards BRC2 and MONGOL garnet were analysed in sampling brackets to 223 the unknowns throughout the session. Precision was calculated at less than 10% relative 224 standard deviation based on 1σ distribution of the presented trace elements.

Page 10 of 61

225

226 Correlative Chemical and Microstructural Analysis

227 Image analysis was performed on the corrected X-ray intensity (wt %) and the EBSD maps to

- 228 correlate and quantify the extent of element zoning associated with low-angle boundary
- 229 development. This analysis was undertaken in MATLAB
- 230 (https://au.mathworks.com/products/matlab.html). Chemically-distinct regions of the mineral
- 231 (for both garnet and omphacite) in the elemental maps were isolated and masked using
- appropriate thresholds (*z*, see below) following methods outlined by Marmo et al. (2002).
- 233 Additional binary masks were created to delineate regions of ehemical change within garnet
- and omphacite and smoothed by a factor of 4 to remove noise below the analytical step size
- 235 (of the element maps). The analysis focused on prominent (metamorphic) elemental zoning,

primarily: for garnet, MgO (z < 5.5 wt %) and CaO (z > 6 wt %); and for omphacite, Na₂O

237 (z < 1.5 wt %), CaO (z < 3.5 wt %O) and Al₂O₃ (z < 1.75 wt %). The binary matrices were

238 rectified to EBSD maps of crystal lattice strain. Euclidean distance measurements were

calculated for three crystal regions with distinct substructure (based on misorientation

240 distributions) and chemistry: (1) igneous cores; (2) metamorphic rims adjacent to high-angle

boundaries but with low lattice distortion ($<1.5^{\circ}$ misorientation/ μ m²); and (3) highly distorted

- 242 metamorphic rims with abundant low-angle boundaries (>1.5° misorientation/ μ m²). The
- 243 effect of fractures and incidental defects in the dataset were reduced by smoothing using
- 244 Fourier transform methods. A defined buffer of 4 pixels (~2 μm) around the low-angle

boundaries was utilised to account for the step size of the EBSD analysis. The Euclidean distances were calculated from the high- and low-angle boundaries to each pixel in regions of elemental change to define the length scales. The calculation produced matrices infilled with an intensity gradient proximal to the boundaries, whether the edge of the chemical zonation. Statistical analysis involved the determination of the mean distance over 250 the defined pixel area to the 1σ level, accounting for the inherent intensity gradient produced 251 in the Euclidean distance maps. These gradients result in the systematically higher standard 252 deviation (σ) in areas with extensive mineral zonation, and therefore does not simply reflect 253 the calculation error. The variance thus provides a measure on the likely extent of the 254 zonation in relation to the interconnectivity of the boundaries. To directly compare the 255 length-scales of zonation associated with high distortion rims (mainly low-angle boundaries) 256 and low distortion rims (mainly high-angle boundaries) a ratio was calculated between the 257 two regions (dl = low-angle boundary distance/high-angle boundary distance). All analyses 258 and map values were converted to micrometres (μ m) from pixels. All the Euclidean distance maps are provided in the supplement (Fig. S1). 259 260

261 **RESULTS**

262 Microstructure and Mineral Chemistry

263 Detailed characterisations of microstructural relations and mineral chemistry are presented

264 for the omphacite granulite elsewhere (De Paoli et al., 2009; Clarke et al., 2013; Chapman et

al. 2015, 2017, submitted; Miranda & Klepeis (2016). This study focuses on relating the

266 mineral chemical variations to recrystallisation microstructure an stal substructure.

267

268 Garnet

269 Large euhedral garnet phenocrysts (1000–3000 μ m: Grt_i) form mm-scale mafic grain cl

270 intergrown with omphacite. The cores of large grains have faceted and euhedral inclusions of

- 271 omphacite and antiperthite in addition to fine rutile exsolution lamellae consiste
- unimpeded igneous growth (Fig. 2a) (after Vernon et al., 2012). In contrast, garnet neoblasts
- 273 (Grt_m) form coronae on attenuated omphacite grain clusters (Figs 2b, c & 3), They have
- rounded and vermicular quartz inclusions and c. 120° hom ase grain triple-junctions (Fig.

Page 12 of 61

275	2c). These features are consistent with late- S_1 metamorphic growth. The outermost parts of
276	most garnet phenocrysts are comparatively grossular-rich and pyrope-poor and are
277	compositionally equivalent to the garnet neoblasts (Fig. 4). The scale and s
278	compositional changes are spatially irregular: polyphase boundaries of garnet and feldspar
279	are commonly marked by a narrow (c. 25–50 μ m) rim of distinct chemistry; polyphase
280	boundaries of garnet with omphacite commonly show minimal or no compositional change;
281	and c. 250–500 μ m-scale, grossular-rich pyrope-poor patches may be associated with
282	inclusion-rich parts of garnet or simply cover broad areas of what are inferred to be relic
283	"phenocryst," (Fig. 4). The narrow rims and irregular larger patches are interpreted as being
284	mostly phenocity and that was chemically modified by element exchange during
285	metamorphism. Polyphase (garnet-feldspar) overgrowths to some large garnet grains include
286	lobate boundaries consistent with metamorphic overgrowth (Fig. 2b). These eoronate
287	intergrowths are more common in higher-strain domains.
287 288	intergrowths are more common in higher-strain domains. Most lattice distortion in garnet is restricted to the relict phenocrysts, with neoblasts
288	Most lattice distortion in garnet is restricted to the relict phenocrysts, with neoblasts
288 289	Most lattice distortion in garnet is restricted to the relict phenocrysts, with neoblasts generally being free of substructure (<2°). Large garnet cores record up to 4° degrees of
288 289 290	Most lattice distortion in garnet is restricted to the relict phenocrysts, with neoblasts generally being free of substructure (<2°). Large garnet cores record up to 4° degrees of crystal lattice distortion that occurs progressively over a distance of ~200–2000 μ m (Figs 3a).
288 289 290 291	Most lattice distortion in garnet is restricted to the relict phenocrysts, with neoblasts generally being free of substructure (<2°). Large garnet cores record up to 4° degrees of crystal lattice distortion that occurs progressively over a distance of ~200–2000 µm (Figs 3a). Small high-strain regions (~300 µm) at elongated grain tips or adjacent to neighbouring
288 289 290 291 292	Most lattice distortion in garnet is restricted to the relict phenocrysts, with neoblasts generally being free of substructure (<2°). Large garnet cores record up to 4° degrees of crystal lattice distortion that occurs progressively over a distance of ~200–2000 μ m (Figs 3a). Small high-strain regions (~300 μ m) at elongated grain tips or adjacent to neighbouring garnet crystals have appreciable lattice misorientation of greater initial (above 20°) (Fig.
288 289 290 291 292 293	Most lattice distortion in garnet is restricted to the relict phenocrysts, with neoblasts generally being free of substructure (<2°). Large garnet cores record up to 4° degrees of crystal lattice distortion that occurs progressively over a distance of ~200–2000 µm (Figs 3a). Small high-strain regions (~300 µm) at elongated grain tips or adjacent to neighbouring garnet crystals have appreciable lattice misorientation of greater in the distortion of greater in the distortion is focussed in a series of closely spaced step-like low-angle
288 289 290 291 292 293 294	Most lattice distortion in garnet is restricted to the relict phenocrysts, with neoblasts generally being free of substructure (<2°). Large garnet cores record up to 4° degrees of crystal lattice distortion that occurs progressively over a distance of ~200–2000 μ m (Figs 3a). Small high-strain regions (~300 μ m) at elongated grain tips or adjacent to neighbouring garnet crystals have appreciable lattice misorientation of greater closely spaced step-like low-angle boundaries (each of 1–5°), with limited or no misorientation between the stepped closely closel
288 289 290 291 292 293 294 295	Most lattice distortion in garnet is restricted to the relict phenocrysts, with neoblasts generally being free of substructure (<2°). Large garnet cores record up to 4° degrees of crystal lattice distortion that occurs progressively over a distance of ~200–2000 µm (Figs 3a). Small high-strain regions (~300 µm) at elongated grain tips or adjacent to neighbouring garnet crystals have appreciable lattice misorientation of greater initiate (above 20°) (Fig. 3a). In detail, most distortion is focussed in a series of closely spaced step-like low-angle boundaries (each of 1–5°), with limited or no misorientation between the stepped inges (Fig. 3d & e). These low-angle boundaries vary in length (200–500 µm) and generally adjoin

- crystallographic orientations (Prior et al., 2002; Cyprch, Piazolo & Almqvist, 2017). A series
 of post-S₁ rectilinear fractures cut some of the garnet grains.
- 301

302 *Omphacite*

303 Omphacite typically forms in complex aggregates with igneous garnet that preserve S_1 flaser 304 structures (Figs 2b–c, e–f & 5). Cores of large omphacite grains (\sim 2000 µm: Omp_i) have 305 faceted plagioclase inclusions and delicate titano-hematite exsolution lamellae (Figs 2e & f). These cores are typically calcic and enveloped by near-concentric jadeite-rich rims ($\mathbf{F}_{\underline{\underline{}}}$) 306 307 that may or may not be coherent with the core. The calcic grains also preserve interlocking 308 euhedral microstructures of low dihedral angles consistent with mutual impingement (fig. 2 309 Chapman et al., 2017). Such features are consistent with these omphacite porphyroclasts 310 mostly reflecting growth from a magma (after Vernon et al., 2012). The phenocrystal-cores are surrounded by hom see polygonal grain aggregates of comparatively calcium-poor 311 312 omphacite (50–400 μ m: Omp_m) formed of smaller high-angle grains with limited internal substructure, most consistent with tamorphic origin (Figs 2e, f & 5, 6; Vernon et al., 313 314 2012). Such neoblastic aggregates are commonly attenuated into flaser tails on igneous garnet 315 or omphacite grains, in places forming high-aspect ratio ribbons (Fig. 2b & e). In all instances, grains forming these neoblastic tails are jade 316 317 igneous grains (Chapman et al., submitted). Omphacite neoblasts with the highest jadeite 318 contents occur in the aggregate tips (Fig. 6). 319 Omphacite porphyroclasts can show pronounced elongation and progressive crystal 320 lattice distortion of up to 12° (Fig. 5a & d). This is distinct from relationships in the fine-321 grained neoblastic aggregates, where grains have minimal internal substructure ($\leq 2^\circ$: Fig. 5a

- 322 & d). Progressive misorientation occurs across large distances in porphyroclastic grain cores
- 323 (>1000 μ m) through a series of step-like low-angle boundaries (~1°) (Fig. 5a & d). The

324 spacing between the low-angle boundaries reduces, and lattice distortion is more focused 325 (4°), towards the elongated edges of the grains (Fig. 5d). A succession of curved low-angle 326 boundaries (100-300 µm in size) concentrate the overall lattice distortion (1-2°) (Fig. 5a). 327 The low-angle boundaries display step-like misorientations separated by regions of 328 progressive distortion ($<1^{\circ}$) (Figs 5a & e). The size of the sub-grain enclosed by the low-329 angle boundaries (\sim 50–400 µm) matches the size of the equant neoblasts that make up the 330 homophase flaser tails (Fig. 5a). The variation in crystallography between these crystals 331 defines a progressive rotation in orientation into the S₁ fabric (Fig. 5c). The majority of 332 dispersion appears to be accommodated by rotation on both the [001] or the [110] axes, 333 consistent with the overall preferred orientations of omphacite (Fig. 5b & c: Brenker, Prior & Müller, 2002; Chapman et al., submitted). 334

335

336 Correlating lattice strain to chemical zonation

337 Major and trace element distinctions between garnet types can be spatially correlated with 338 crystal substructure. Calcium and magnesium zoning in garnet is more extensively developed 339 in localized crystal volumes that record appreciable distortion. The length scales of modified 340 (i.e. metamorphic) Ca and Mg compositions in regions of abundant low-angle boundaries 341 (distorted regions) ranges from near parity with, to up to 2.5 times greater than, that recorded 342 by high-angle rims with limited lattice distortion (dl: Fig. 7). This is reflected in the 343 systematically higher mean distances in the lattice regions with appreciable distortion (Fig. 344 7). Together with the higher standard deviation (σ) from these domains (Fig. 7), the 345 calculations reflect greater length scales of diffusion related to crystal plastic strain and imply 346 that the crystallographic boundaries were at least partially interconnected in 3D. Grain size 347 has no appreciable influence on the scale of chemical change; in all grains, the average 348 distance from igneous cores to regions of chemical change is similar. The result represents

the overall maximum length scale of intra-crystalline diffusion from both high- and low-angle boundary networks (Fig. 7).

351	Correlations between regions of chemical change and the development of low-angle
352	boundaries in omphacite are less distinct. Typically, zoning in omphacite has a regular
353	concentric habit. There is no apparent dependence between the extent of zoning and grain
354	size of the porphyroclast (Fig. 8). Generally, areas of comparatively calcic omphacite have
355	similar length scales (mean d ces and d/ ratios) in both low- and high-angle boundary
356	regions. The length scales for Na and Al zonation in regions with abundant low-angle
357	boundaries (high distortion) is greater ($dl = 1.1-1.6$) consistent with subtly more extensive
358	change (metamorphism) (Fig. 8). These differences between elements are also apparent in the
359	variance (σ), which is high br Na and Al compared with Ca. The observations would
360	appear to indicate that the low-angle boundaries provided the greatest influence on Na and Al
361	diffusion, in association with the interconnected nature of the crystallographic boundaries in
362	3D. However, this affect is less pronounced in omphacite than in garnet.
363	The influence of crystal plastic strain on intra-grain trace element diffusion can be
364	broadly assessed through spatial trends in concentration. At the first order, highly distorted
365	regions of garnet have lower concentrations of Zr and Ti, but similar Y content, when
366	compared with grain rims that lack lattice distortion (Fig. 9). Other transition metals, such as
367	Cr and Ni, record a general decrease in concentration from the core to the rim of garnet
<mark>368</mark>	grains, similar to variations in elemental concentration in regions recording crystal lattice
369	strain (Figs 9 & S2). A centric style of zoning is apparent for some trace elements in
370	omphacite: Ti, Nd and Sr content transitions in a generally linear fashion from high core
371	concentrations to low rim concentrations (Figs 10 & S3 for Mn & Zr). However, areas with
372	the lowest concentrations tend to occur in neoblasts or grain regions with abundant low-angle
373	boundaries (Fig. 10). Chromium concentration increases progressively towards the rim, with

the highest concentrations in the distorted regions with abundant low-angle boundaries, but

the lowest concentrations are generally observed in neoblasts (Fig. 10b). Nickel

376 concentrations are largely consistent (~140 ppm) throughout crystal form (core, rim or

neoblasts) (Fig. 10c).

378

379 **DISCUSSION**

380 High-grade metamorphic rocks commonly preserve grain-scale variability in microstructures

381 and mineral chemistry that reflect dynamic changes in intrinsic and/or extrinsic variables

including recrystallization (Powell et al., 2005; Williams & Jercinovic, 2012). In the

383 Breaksea Orthogneiss, there is a marked grain-scale association between deformation

384 microstructure and metamorphic reaction. Low-strain regions commonly preserve

385 phenocrysts of omphacite and garnet with delicate microstructural and chemical features

retained from the high-*T* recrystallization of the igneous protolith (*T*>1000°C), such as

387 exsolution lamellae and facetted inclusions (Clarke et al., 2013; Chapman et al., 2017). Rims

388 to porphyroclasts and neoblastic minerals in high-strain domains have ehemical compositions

that match better predictions from mineral equilibria modelling of metamorphosed

390 intermediate protoliths at the inferred peak conditions (~850°C, 1.8 GPa: De Paoli et al.,

391 2012; Chapman et al., 2017). The occurrence of domainal metamorphic equilibration in

392 regions of high-strain and the generation of gneissic foliation is common to other high-grade

terranes (e.g. Austrheim, 1987; Williams, Dumond, Mahan, Regan & Holland, 2014). The

394 spatial association begs the question as to what variables control this dependency at the grain-

395 scale? Establishing this context becomes particular relevant in extracting appropriate

information to establish plausible petrogenetic histories (e.g. Vernon et al., 2008; cf. Stowell

397 et al., 2017).

398

399	Low-angle boundary networks as elemental pathways of enhanced diffusivity
400	An intrinsic link between recrystallisation and metamorphic reaction progress in the Breaksea
401	Orthogneiss can mostly account for the grain-scale development of comparatively grossular-
402	rich garnet, jadeite-rich omphacite, clinozoisite and kyanite, and the consumption of
403	plagioclase. Peripheral regions of the porphyroclasts preserve the patchy chemical
404	modification of igneous grains, in sites associated with crystal plastic strain (Figs 4 & 6).
405	Igneous garnet cores with only subtle misorientation are enclosed by metamorphic rims of
406	higher grossular content; rims are very narrow where the magnitude of lattice misorientation
407	is low (~0-3°), and more extensively developed in areas with abundant 3D defects forming
408	low-angle (~4-10°) boundary networks and sub-grains. Similarly, omphacite cores are
409	enclosed by narrow metamorphic rims of higher jadeite content where lattice misorientation
410	is low, and subtly wider rims in areas with extensive distortion and low-angle boundary
411	development (misorientation steps of $\sim 2^{\circ}$: Figs 5 & 6). The scale and site of the
412	compositional changes in regions of plastic strain in the Breaksea Orthogneiss reflects a
413	dependency of grain-scale metamorphism, on the time-scales involved in this example
414	through intra-crystalline diffusion on the generation of low-angle boundaries (Figs 7 & 8).
415	The pronounced coupling of grain-scale change and the development of low-angle
416	boundaries could reflect the development of either: (1) enhanced diffusion pathways
417	associated with the clustering of crystalline defects following recovery from strain related to
418	far-field stress; or (2) chemical modification generating lattice volume strain. Distinguishing
419	the role of these mechanisms is dependent on the timing of deformation relative to the
420	observed chemical transformation. In the Breaksea Orthogneiss, the presence of growth
421	zoning in garnet and omphacite neoblasts is consistent with deformation having generally
422	preceded most chemical change. In addition, in lower-strain samples, garnet has grossular-
423	rich overgrowths that lack any accompanying substructure (Fig. 2d). Examples of zoning in

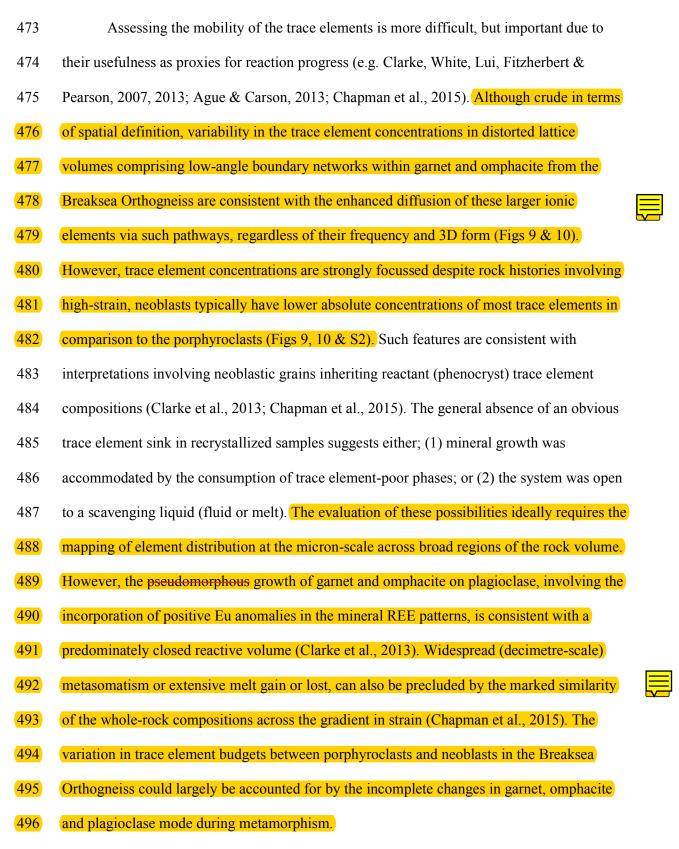
Page 18 of 61

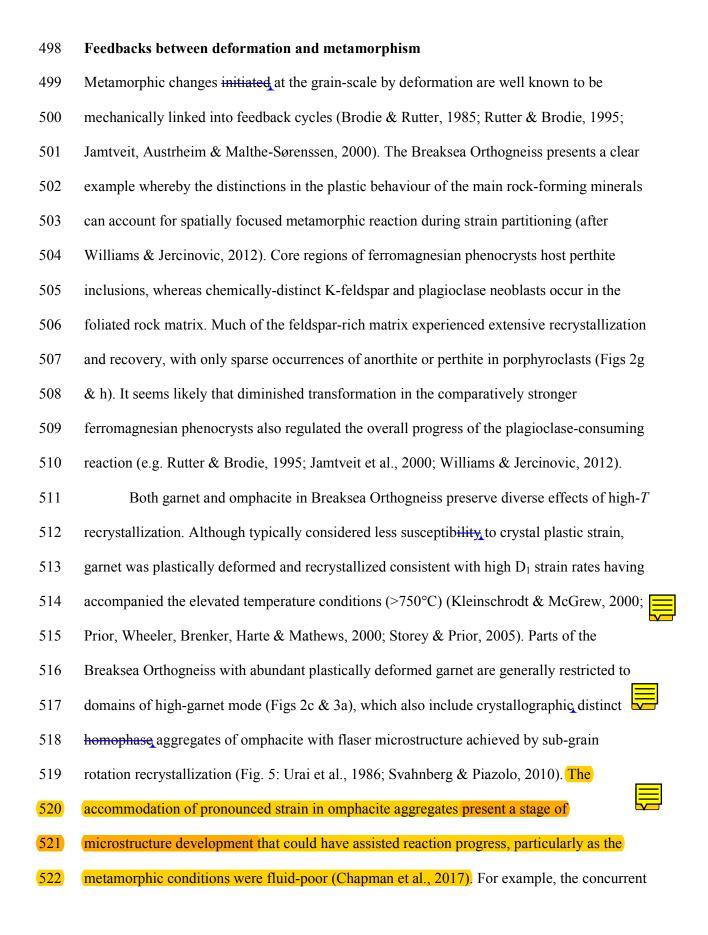
plastically-strained garnet and omphacite from Breaksea Sound are inferred to reflect the
enhancement of element mobility in relation to crystal substructure. It is envisaged that the
activation of pipe diffusion, along the cores of dislocation arrays (low-angle boundaries)
contributed to the complex zonal patterns (e.g. Hart, 1957; Love, 1964; Lund et al., 2006;
Piazolo et al., 2012, 2016). However, feedback associated with internal volume adjustment
and lattice strain recovery may also have subsequently transpired (White & Knipe, 1978;
Rutter & Brodie, 1985).

431 The activation of pipe diffusion in crystal regions of enhanced plastic strain increase 432 the propensity of extensive grain-scale zonation (Fig. 11) (Reddy et al., 2006; Piazolo et al., 2016). The length scale of chemical motor ation in distorted lattice volumes with low-angle 433 434 boundary networks in garnet from the Breaksea Orthogneiss is more than 1.5-2.5-times (dl) 435 greater than the length scales associated with zoning from the grain edge lacking lattice 436 distortion (Fig. 8). In omphacite, this association is less pronounced: distorted low-angle 437 boundary networks are associated with only marginally greater (dl = 1-1.6-times) length 438 scales of Na and Al zoning compared to that in the undistorted grain rims (Fig. 9). The 439 differing capacity of the low-angle boundaries to act as pathways for element movement in 440 minerals will relate in part to their configuration (e.g. Storey & Prior, 2005). The distinction 441 in style of (1) step-like lattice distortion along low-angle boundaries in garnet, compared to 442 (2) more graduated misorientation in omphacite, is consistent with differing compatibilities 443 of internal strain accommodation by the two minerals during recovery (Figs 3 & 5; Piazolo, 444 Bestman, Prior & Spiers, 2006). The migration of dislocations into low-angle arrays appears 445 to have been more efficient in garnet than in omphacite (e.g. Urai et al., 1986; Piazolo et al., 446 2006). It is likely that the frequency of 3D interconnection between low-angle boundaries 447 was also greater in garnet. The creation of a low-angle boundary network with recovered sub-

grains would contribute to the general effectiveness of mineral substructure to act as elementpathways in conjunction with standard diffusion from the grain-edge.

450 The relatively rate of strain (or recovery) compared to reaction progress and diffusion 451 also becomes relevant in assessing the proficiency of crystal substructure to transform 452 minerals (e.g. Baxter & DePaolo, 2003). It can be assumed, based on empirical theory, that 453 diffusion along dislocation "pipes" proceeds at a rate intermediate to that of intracrystalline-454 and grain boundary diffusion (Hart, 1957; Ruoff & Balluffi, 1963; Love, 1964; Yardley, 455 1977). Assessments of metamorphic duration are, however, based primarily on models of 456 grain growth via standard ionic diffusion simply from the grain edge (e.g. Lasaga, 1979; 457 Ague & Carson, 2013; Stowell et al., 2017). Major element relationships preserved in 458 omphacite and garnet in the Breaksea Orthogneiss are consistent with low-angle boundary 459 networks having enhanced the length scales of diffusion in common metamorphic exchange 460 reactions. Less deformed grains that lack interconnected low-angle boundary networks show 461 only limited peripheral chemical modification on account of the slower rates of intra-462 crystalline diffusion, most likely controlled by poorly linked defects (Fig. 11). Extensive 463 plastic deformation, and recovery, appears to have enhanced element mobility through the 464 development of low-angle boundaries, resulting in heterogeneous zoning during high-T 465 metamorphism (see also Piazolo et al., 2016). This influence of crystal plastic strain on the length-scales of major element diffusion would also have the effect of up-s 466 467 extent of element exchange between the rock-forming minerals (and any liquid present) 468 during a given metamorphic event, commonly referred to as the effective equilibrium volume 469 (e.g Stüwe, 1997; Marmo et al., 2002; White, Powell & Baldwin, 2008; Schorn & Diener, 470 2017). The capacity of minerals to respond to changes in extrinsic variables through major 471 element diffusion, in the example of the Breaksea Orthogneiss, was dependent on the 472 partitioning and related time-scales of D₁ strain during subsolidus cooling.





Page 22 of 61

523 attenuation and reduction in grain size of omphacite into flaser structures would help increase 524 the proficiency of reactive volumes with higher densities of grain boundaries (Fig. 6; e.g. 525 Yund & Tullis, 1991). In addition, the flaser microstructures would present suitable sites for 526 the preferential nucleation of garnet coronae, possibly activated by both local chemical 527 potential gradients and attempts to minimise strain energy (Figs 2b, 3 & 4; Stünitz 1998; 528 Satsukawa et al., 2015; Smith, Piazolo, Daczko & Evans, 2015). 529 Causal dependencies between metamorphism and recrystallization during the D₁ 530 deformation presents a simple explanation for the focussed nature of the reaction 531 relationships. However, intrinsic feedbacks between metamorphism and deformation in rocks 532 like the Breaksea Orthogneiss can potentially be complicated through ongoing dilation or 533 compression (White & Knipe, 1978; Vernon, 1998). Volume changes induced by either phase 534 transformation or deformation are likely to be intimately linked into a feedback cycle that 535 continues to partition strain and reaction. Volume change in the Breaksea Orthogneiss was 536 heterogeneous on a metre to millimetre-scale. The theoretical densification of the 537 monzodioritic protolith at the peak metamorphic conditions (850°C, 1.8 GPa) would result in 538 a negative molar volume change of $\sim 4.34\%$ (=0.9102 cm³/per mole: after Chapman et al., 539 2017). The restricted growth of omphacite can account for most of this change, but would 540 appear to have been transiently dependent on deformation (see also Tajčmanová et al., 2014; Wheeler, 2014; Powell et al., 2005) 541

542

543 CONCLUSIONS

544 A discernible grain-scale dependency between metamorphic reaction and deformation is

observed in granulite and eclogite components of the Breaksea Orthogneiss. Crystal plastic

546 deformation in garnet and omphacite localised reaction at the grain scale, but metamorphic

547 change in the feldspathic matrix was more extensive and linked to greater strain, in tra-

548	crystalline element mobility within garnet and omphacite was enhanced, by up to 2
549	length scale, along low-angle boundary networks in formerly homogeneous silicates. There
550	was only comparatively limited change along grain margins (high-angle boundaries).
551	
552	ACKNOWLEDGMENTS
553	Analytical funding for this project was provided by internal funding to GLC from the School
554	of Geosciences, the University of Sydney, and through Australian Research Council Funding
555	(DP120102060 and Future Fellowship FT1101100070 to SP). The Department of
556	Conservation in Te Anau is thanked for permission to visit and sample localities at Breaksea
557	Sound, Fiordland National Park. This research was supported and aided by technical
558	assistance of N. Butterworth of the Sydney Informatics Hub, a core facility that is funded by
559	the University of Sydney. The authors also acknowledge the facilities, scientific and technical
560	assistance of the Australian Microscopy & Microanalysis Research Facility at the Australian
561	Centre for Microscopy & Microanalysis at the University of Sydney as well as K. Goeman at
562	The University of Tasmania. This is contribution XX from the ARC Centre of Excellence for
563	Core to Crust Fluid Systems (http://www.CCFS.mq.edu.au) and XX from GEMOC
564	(http://www.GEMOC.mq.edu.au). The analytical data were obtained using instrumentation
565	funded by DEST Systemic Infrastructure Grants, ARC LIEF, NCRIS, industry partners and
566	Macquarie University.
567	
568	REFERENCES

- 569 Ague, J. J. & Carson, W. D. (2013). Metamorphism as garnet sees it: the kinetics of
- 570 nucleation, equilibration, and diffusional relaxation. *Elements*, **9**, 439–445.
- 571 Allibone, A. H., Jongens, R., Turnbull, I. M., Milan, L. A., Daczko, N. R., De Paoli, M. C. &
- 572 Tulloch, A. J. (2009). Plutonic rocks of western Fiordland, New Zealand: field

- 573 relations, geochemistry, correlation and nomenclature. New Zealand Journal of
- 574 Geology and Geophysics, 52, 379–415.
- Austrheim, H. (1987). Eclogitization of lower crustal granulites by fluid migration through
 shear zones. *Earth and Planetary Science Letters*, **81**, 221–232.
- 577 Baxter, E. F. & De Paolo, D. J. (2003). Can metamorphic reactions proceed faster than bulk
 578 strain? *Contributions to Mineralogy and Petrology*, **146**, 657–670.
- Betka, P. M. & Klepeis, K. A. (2013). Three-stage evolution of lower crustal gneiss domes at
 Breaksea Entrance, Fiordland, New Zealand. *Tectonics*, **32**, 1084–1106.
- 581 Bürgmann, R. & Dresen, G. (2008). Rheology of the lower crust and upper mantle: evidence
- from rock mechanics, geodesy, and field observations. *Annual Reviews of Earth and Planetary Sciences*, 36, 531–567.
- 584 Bradshaw, J. Y. (1989). Origin and metamorphic history of an Early Cretaceous polybaric
- granulite terrain, Fiordland, southwest New Zealand. *Contributions to Mineralogy and Petrology* 103, 346–360.
- 587 Brenker, F. E., Prior, D. J. & Müller, W. F. (2002). Cation ordering in omphacite and effect
 588 on deformation mechanism and lattice preferred orientation (LPO). *Journal of*
- 589 *Structural Geology*, **24**, 1991–2005.
- 590 Brodie, K. H. & Rutter, E. H. (1985). On the relationships between deformation and
- 591 metamorphism, with special reference to behaviour of basic rocks. *In*, Thompson, A.
- 592B. & Rubie, D. C. (Eds.) Advances in Physical Geochemistry. Springer–Verlag, New
- 593 York, 138–179.
- 594 Chapman, T., Clarke, G. L., Daczko, N. R., Piazolo, S. & Rajkumar, A. (2015).
- 595 Orthopyroxene–omphacite- and garnet–omphacite-bearing magmatic assemblages,
- 596 Breaksea Orthogneiss, New Zealand: oxidation state controlled by high-*P* oxide
- 597 fractionation. *Lithos*, **216–217**, 1–16.

598	Chapman, T., Clarke, G. L. & Daczko, N. R. (2016). Crustal differentiation in a thickened arc
599	- evaluating depth dependencies. Journal of Petrology, 57, 595-620.
600	Chapman, T., Clarke, G. L., Piazolo, S. & Daczko, N. R. (2017). Evaluating the importance
601	of metamorphism in the foundering of continental crust. Scientific Reports 7,
602	DOI:10.1038/s41598-017-13221-6.
603	Chapman, T., Clarke, G. L., Piazolo, S. & Daczko, N. R. (submitted). Quantifying the
604	proportions of relict igneous and metamorphic minerals in variably strained
605	orthogneiss. American Mineralogist.
606	Clarke, G. L., Daczko, N. R. & Nocklods, C. (2001). A method for applying matrix
607	corrections to X-ray intensity maps using Bence-Albee algorithm and MATLAB.
608	Journal of Metamorphic Geology, 19, 635–644.
609	Clarke, G. L., White, R. W., Lui, S., Fitzherbert, J. A. & Pearson, N. J. (2007). Contrasting
610	behaviour of rare earth and major elements during partial melting in granulite facies
611	migmatites, Wuluma Hills, Arunta Block, central Australia. Journal of Metamorphic
612	<i>Geology</i> , 25 , 1–18.
613	Clarke, G. L., Daczko, N. R. & Miescher, D. (2013). Identifying relict igneous garnet and
614	clinopyroxene in eclogite and granulite, Breaksea Orthogneiss, New Zealand. Journal
615	of Petrology, 54 , 1921–1938.
616	Cottrell, A. H. (1953). Theory of dislocations. Progress in Metal Physics, 4, 205–264.
617	Cyprych, D., Piazolo, S. & Almqvist, B. S. G. (2017). Seismic anisotropy from compositional
618	banding in granulites from deep magmatic arc of Fiordland, New Zealand. Earth and
619	Planetary Science Letters, 477, 156–167.
620	De Paoli, M. C., Clarke, G. L., Klepeis, K. A., Allibone, A. H. & Turnbull, I. M. (2009). The
621	eclogite-granulite transition: mafic and intermediate assemblages at Breaksea Sound,
622	New Zealand. Journal of Petrology, 50, 2307–2343.

623	De Paoli, M. C., Clarke, G. L. & Daczko, N. R. (2012). Mineral equilibria modeling of the
624	granulite-eclogite transition: effects of whole-rock composition on metamorphic
625	facies type-assemblages. Journal of Petrology, 53, 949-970.
626	Hart, E. W. (1957). On the role of dislocations in bulk diffusion. Acta Metallurgica, 5, 597.
627	Hasalová, P., Schulmann, K., Lexa, O., Štípská, P., Hrouda, F., Ulrich, S., Haloda, J. &
628	Týcová, P. (2008). Origin of migmatites by deformation-enhanced melt infiltration of
629	orthogneiss: a new model based on quantitative microstructural analysis. Journal of
630	Metamorphic Geology, 26, 29–53.
631	Jamtveit, B., Austrheim, H. & Malthe-Sørenssen, A. (2000). Accelerated hydration of the
632	Earth's deep crust induced by stress perturbations. Nature, 408, 75-78.
633	Kleinschrodt, R. & McGrew, A. (2000). Garnet plasticity in the lower contiental crust:
634	implications for deformation mechanisms based on microstructures and SEM-electron
635	channeling pattern analysis. Journal of Structural Geology, 22, 795-809.
636	Klepeis, K. A., Schwartz, J., Stowell, H. & Tulloch, A. J. (2016). Gneiss domes, vertical and
637	horizontal mass transfer, and the initiation of extension in the hot lower-crustal root of
638	a continental arc, Fiordland, New Zealand. Lithosphere, 8, 116-140.
639	Lasaga, A. C. (1979). Multicomponent exchange and diffusion in silicates. Geochimica et
640	<i>Cosmochimica Acta</i> , 43 , 455–469.
641	Love, G. R. (1964). Dislocation pipe diffusion. Acta Metallurgica, 12, 731–737.
642	Love, G. & Scott, V. D. (1978). Evaluation of new correction procedure for quantitative
643	electron probe micro analysis. Journal of Physics, 11, 1369–1376.
644	Legros, M., Dehm, G., Arzt, E. & Balk, T. J. (2008). Observation of giant diffusivity along

645 dislocations cores. *Science*, **319**, 1646–1649.

646	Lund, M. D., Piazolo, S. & Harley, S. L. (2006). Ultrahigh temperature deformation
647	microstructures in felsic granulites of the Napier Complex, Antarctica.
648	<i>Tectonophysics</i> , 427 , 133–151.
649	Marmo, B. A., Clarke, G. L. & Powell, R. (2002). Fractionation of bulk rock composition due
650	to porphyroblast growth: effects of eclogite facies mineral equilibria, Pam Peninsula,
651	New Caledonia. Journal of Metamorphic Geology, 20, 151–165.
652	Milan, L. A., Daczko, N. R., Clarke, G. L. & Allibone, A. H. (2016). Complexity of in situ U
653	Pb–Hf isotope systematics during arc magma genesis at the roots of a Cretaceous arc,
654	Fiordland, New Zealand. Lithos, 264, 296-314.
655	Milan, L. A., Daczko, N. R. & Clarke, G. L. (2017). Cordillera Zealandia: A Mesozoic arc
656	flare-up on the palaeo-Pacific Gondwana margin. Scientific Reports, DOI:
657	10.1038/s41598-017-00347-w.
658	Miranda, E. A. & Klepeis, K. A. (2016). The interplay and effects of deformation and
659	crystallized melt on the rheology of the lower continental crust, Fiordland, New
660	Zealand. Journal of Structural Geology, 93, 91–105.
661	Piazolo, S., Bestmann, M., Prior, D. J. & Spiers, C. J. (2006). Temperature dependent grain
662	boundary migration in deformed-then-annealed material: observations from
663	experimentally deformed synthetic rocksalt. Tectonophysics, 427, 55-71.
664	Piazolo, S., Austrheim, H. & Whitehouse, M. (2012). Brittle-ductile microfabrics in naturally
665	deformed zircon: deformation mechanisms and consequences for U-Pb dating.
666	American Mineralogist, 97, 1544–1563.
667	Piazolo, S., La Fontaine, A., Trimby, P., Harley, S., Yang, L., Armstrong, R. & Cairney, J.
668	(2016). Deformation-induced trace element redistribution in zircon revealed using
669	atom probe tomography. Nature Communications, DOI: 10.1038/ncomms10490.

670	Powell, R. Guiraud, M. & White, R. W. (2005). Truth and beauty in metamorphic phase
671	equilibria: conjugate variables and phase diagrams. The Canadian Mineralogist, 43,
672	21–33.
673	Powell, R. & Holland, T. J. B. (2008). On thermometry. Journal of Metamorphic Geology,
674	26 , 155–179.
675	Powell, R., Evans, K. A., Green, E. C. A. & White, R. W. (2017). On equilibrium in non-
676	hydrostatic systems. Journal of Metamorphic Geology, DOI: 10.1111/jmg.12298.
677	Prior, D. J., Boyle, A. P., Brenker, F., Cheadle, M. C., Day, A., Lopez, G., Peruzzo, L., Potts,
678	G. J., Reddy, S., Spiess, R., Timms, N. E., Trimby, P., Wheeler, J. & Zetterström, L.
679	(1999). The application of electron backscatter diffraction and orientation contrast
680	imaging in the SEM to textural problems in rocks. American Mineralogist, 84, 1741-
681	1759.
682	Prior, D. J., Wheeler, J., Brenker, F. E., Harte, B. & Mathews, M., 2000. Crystal plasticity of
683	natural garnet: new microstructural evidence. Geology, 28, 1003-1006.
684	Prior, D. J., Wheeler, J., Peruzzo, L., Spiess, R. & Storey, C. (2002). Some garnet
685	microstructures: an illustration of the potential of orientation maps and misorientation
686	analysis in microstructural studies. Journal of Structural Geology, 24, 999-1011.
687	Reddy, S. M., Timms, N. E., Trimby, P., Kinny, P. D., Buchan, C. & Blake, K. (2006).
688	Crystal-plastic deformation of zircon: a defect in the assumption of chemical
689	robustness. Geology, 34 , 257–260.
690	Ruoff, A. L. & Balluffi, R. W. (1963). Strain-enhanced diffusion in metals. II. Dislocation
691	and grain-boundary short-circuiting models. Journal of Applied Physics, 34, 1848-
692	1854.
693	Rutter, E. H. & Brodie, K. H. (1995). Mechanistic interactions between deformation and
694	metamorphism. Geological Journal, 30, 227–240.

695	Satsukawa, T., Piazolo, S., González-Jiménez, J. M., Colás, V., Griffin, W. L., O'Reilly, S.
696	Y., Gervilla, F., Fanlo, I. & Kerestedjian, T. N. (2015). Fluid-present deformation aids
697	chemical modification of chromite: insights from chromites from Golyamo
698	Kamenyane, SE Bulgaria. Lithos, 228–229, 78–89.
699	Schorn, S. & Diener, J. F. A. (2017). Details of the gabbro-to-eclogite transition determined
700	from microtextures and calculated chemical potential relationships. Journal of
701	Metamorphic Geology, 35 , 55–75.
702	Smith, J. R., Piazolo, S., Daczko, N. R. & Evans, L. (2015). The effect of pre-tectonic
703	reaction and annealing extent on behaviour during subsequent deformation: Insights
704	from paired shear zones in the lower crust of Fiordland, New Zealand. Journal of
705	Metamorphic Geology, 33 , 557–577.
706	Storey, C. D. & Prior, D. J. (2005). Plastic deformation and recrystallisation of garnet: a
707	mechanism to facilitate diffusion creep. Journal of Petrology, 46, 2593-2613.
708	Stüwe, K. (19970. Effective bulk composition changes due to cooling: a model predicting
709	complexities in retrograde reaction textures. Contributions to Mineralogy and
710	<i>Petrology</i> , 129 , 43–52.
711	Stünitz, H. (1998). Syndeformational recrystallisation — dynamic or compositionally
712	induced? Contributions to Mineralogy and Petrology, 131, 219-236.
713	Stowell, H., Schwartz, J. J., Klepeis, K. A., Hout, C., Tulloch, A. J. & Koenig, A. (2017).
714	Sm-Nd ages for granulite and eclogite in the Breaksea Orthogneiss and widespread
715	granulite facies metamorphism in the lower crust, Fiordland magmatic arc, New
716	Zealand. Lithosphere, DOI: 10.1130/L662.1.
717	Svahnberg, H. & Piazolo, S., 2010. The initiation of strain localization in plagioclase-rich
718	rocks: insights from detailed microstructural analyses. Journal of Structural Geology,
719	32 , 1404–1416.

720	Tajčmanová, L., Podladchikov, Y., Powell, R., Moulas, E., Vrijmoed, J. C. & Connelly, J. A.
721	D. (2014). Grain-scale pressure variations and chemical equilibrium. Journal of
722	Metamorphic Geology, 32 , 195–207.
723	Urai, J. L., Means, W. D. & Lister, G. S. (1986). Dynamic recrystallisation of minerals. In
724	Hobbs, B. E., Heard, H. C. (Eds.). Mineral and rock deformation (laboratory studies).
725	Geophysical monograph of the American Geophysical Union, 36, pp. 161–200.
726	Wheeler, J. (2014). Dramatic effects of stress on metamorphic reactions. <i>Geology</i> , 42 , 647–
727	650.
728	White, S. H. & Knipe, R. H. (1978). Transformation- and reaction-enhanced ductility in
729	rocks. Journal of the Geological Society of London, 135, 513–516.
730	White, R. W., Powell, R. & Baldwin, J. A. (2008). Calculated phase equilibria involving
731	chemical potentials to investigate the textural evolution of metamorphic rocks.
732	Journal of Metamorphic Geology, 26, 181–198.
733	Williams, M. L. & Jercinovic, M. J. (2012). Tectonic interpretation of metamorphic
734	tectonites: integrating compositional mapping, microstructural analysis and in situ
735	monazite dating. Journal of Metamorphic Geology, 30, 739-752.
736	Williams, M. L., Dumond, G., Mahan, K., Regan, S. & Holland, M. (2014). Garnet-forming
737	reactions in felsic orthogneiss: implications for densification of the lower continental
738	crust. Earth and Planetary Science Letters, 405, 207–219.
739	Vernon, R. H. (1998). Chemical and volume changes during deformation and prograde
740	metamorphism of sediments In Treloar P. J. & O'Brien P. J. (Eds). What drives
741	metamorphism and metamorphic reactions? Geological Society of London Special
742	Publications, 138 , 215–246.

743	Vernon, R. H., White, R. W. & Clarke, G. L. (2008). False metamorphic events inferred from
744	misinterpretation of microstructural evidence and P-T data. Journal of Metamorphic
745	<i>Geology</i> , 26 , 437–449.
746	Vernon, R. H., Collins, W. J. & Cook, N. D. J. (2012). Metamorphism and deformation of
747	mafic and felsic rocks in a magma transfer zone, Stewart Island, New Zealand.
748	Journal of Metamorphic Geology, 30 , 473–488.
749	Yardley, B. W. D. (1977). An emprical study of diffusion in garnet. American Mineralogists,
750	62 , 793–800.
751	Yund, R. A. & Tullis, J. (1991). Compositional changes of minerals associated with dynamic
752	recrystallisation. Contributions to Mineralogy and Petrology, 108, 346-355.
753	
754	FIGURE CAPTIONS
755	Figure 1 Simplified geological map of the Breaksea Sound area between northern Resolution
756	Island and Coal River (after Chapman et al., 2017). Circles represent sample locations.
757	Abbreviations are Resolution Island Shear Zone and Straight River Shear Zone. Inset shows
758	location of the field area in relation to the South Island geology.
759	Figure 2a Large igneous garnet (Grt _i) containing facetted inclusions of omphacite,
760	antiperthite, plagioclase and rutile. Antiperthite inclusions are intergrown with K-feldspar.
761	The garnet core is defined by rutile exsolution needles (arrow). b Highly strained mafic grain
762	clusters defined by ribbons (arrow) or attenuated omphacite (Omp_m) and garnet neoblasts
763	(Grt_m) that are intergrown with quartz and rutile. c Recrystallisation transition from large
764	elongated igneous garnet (Grt_i) with abundant rutile exsolution to garnet neoblasts (Grt_m)
765	with vermicular inclusions on the each of grain cluster. d Igneous garnet core (Grt _i)
766	surrounded by optically distinct metamorphic overgrowth defined by lobate boundaries
767	(labelled Grt_m). e-f Large igneous omphacite (Omp_i) containing cores with titano-haematite

Page 32 of 61

768 lamellae (Ti-Hem) and facetted plagioclase inclusions (Pl). Surrounding the porphyroclasts 769 are small aggregates of homophase omphacite defining flaser tails (Omp_m). g Granoblastic 770 feldspar-rich matrix displaying 120° triple (arrow) and albite deformation twins (grain 771 labelled Pl). h Graphic intergrowths of plagioclase and K-feldspar within the feldspar-rich 772 matrix. 773 Figure 3a EBSD misorientation map for a garnet recrystallisation microstructure (shown in 774 Fig. 2c) of elongate igneous garnet (white core) transitioning to garnet neoblasts (right). The 775 false colour displays the magnitude of crystallographic distortion (°) relative to an arbitrary 776 point (cross) of the same mineral within the analysis region. Inset, high resolution 777 misorientation map of high-strain region in garnet (shown in red) with prominent low-angle 778 boundaries. **b** Lattice dispersion pattern from boxed area marked in (a); note the clear small 779 circle dispersion of most axes, except <100> which represents the rotation axis. c-d 780 Misorientation profile showing gradual lattice distortion and low-angle boundaries in regions 781 (arrows) transition from igneous garnet to metamorphic overgrowths, line locations and 782 colours correspond to misorientation map (a). 783 Figure 4 Matrix corrected X-ray maps of Mg (a), Fe (b) and Ca (c) in garnet. Only analyses 784 of garnet are shown in the maps (wt % Oxide) for the purpose of showing the pronounced 785 patchy zonation corresponding to highly distorted crystal regions (d). 786 Figure 5a EBSD misorientation map for a omphacite flaser microstructure, across elongated 787 porphyroclast and homophase neoblastic aggregates. The false colour displays the magnitude 788 of crystallographic distortion (°) relative to an arbitrary point (cross) of the same mineral 789 within the analysis region. Inset, high resolution misorientation map of low-angle boundary 790 domain in omphacite (shown in red). b Lattice dispersion pattern from boxed area marked in 791 (a); note the clear small circle dispersion of most axes, except [001] and [110] which 792 represent the rotation axes. **c–d** Misorientation profile showing gradual lattice distortion and

- 793 low-angle boundaries (arrows) in porphyroclast domains and neoblasts, line locations and
- colours correspond to misorientation map.
- Figure 6 Matrix corrected X-ray maps of Al (a), Na (b), Mg (c) and Ca (d) in omphacite (Fig.
- 4). Only analyses of omphacite are shown in the maps (wt % Oxide) for the purpose of
- showing the pronounced patchy zonation. The misorientation map displaying crystal plastic
- strain of this region is shown in Figure 5a.
- 799 Figure 7 Histogram of mean distance calculations of chemical zonation, (a) Ca and (b) Mg,
- 800 associated with cores, highly distorted regions (abundant low-angle boundary networks,
- $>1.5^{\circ}$ misorientation/ μ m²) and low distortion rims (<1.5° misorientation/ μ m²) in garnet. Error
- bars represent 1σ and d*l* is the ratio of distance between highly distorted regions and low
- 803 distortion rims.
- 804 Figure 8 Histogram of distance calculations of zoning, (a) Ca, (b) Na and (c) Al), associated
- 805 with cores, highly distorted regions (abundant low-angle boundary networks, >1.5°
- 806 misorientation/ μ m²) and low distortion rims (<1.5° misorientation/ μ m²) in clinopyroxene.
- 807 Error bars represent 1σ and dl is the ratio of distance between highly distorted regions and
- 808 low distortion rims.
- 809 Figure 9 Bivariate plots (versus Y) of the trace element concentrations in garnet across
- 810 distinct substructural domains: (a) Cr, (b) Ti, (c) Zr and (d) Ni. Error bars represent 1σ
- 811 relative standard deviation on each analysis.
- 812 Figure 10 Bivariate plots (versus Ti) of the trace element concentrations in omphacite across
- 813 distinct substructural and microstructural domains: (a) Sr, (b) Cr, (c) Ni and (d) Nd. Error
- 814 bars represent 1σ relative standard deviation on each analysis.
- 815 Figure 11 Schematic diagram of zoning style associated with the generation of 3D low-angle
- 816 boundary networks during crystal plastic strain (b) versus standard flux diffusion in

Page 34 of 61

- homogeneous garnet (a). Both mechanisms occur concurrently within deformed crystals ofthe Breaksea Orthogneiss.
- 819

820 **Supplementary Table 1** Trace element mineral chemistry (LA-ICPMS) of garnet and 821 omphacite.

822

823 Supplementary Figure 1 Summary Finineral misorientation and elemental correlation

analysis for garnet and omphacite. The false colour EBSD maps display the magnitude of

825 crystallographic distortion (°) relative to an arbitrary point (cross) of the same mineral within

the analysis region. Elemental analyses of garnet or omphacite in (wt % O) show patchy

827 zonation corresponding to regions of crystal plastic strain. Euclidean distance maps associate

the extent of zonation in garnet and omphacite to the crystalline regions with (1) high

distortion and abundant low-angle boundaries and (2) low lattice distortion rims (marked).

830

831 Supplementary Figure 2 Gd_N/Yb_N versus Eu^* (= $Eu_N/\sqrt{Sm_NGd_N}$) diagram of garnet

832 substructural composition (cf. Clarke et al., 2013).

833

834 Supplementary Figure 3 Bivariate plots (*versus* Ti) of the trace element concentrations in

835 omphacite across distinct substructural and microstructural domains: (a) Mn and (b) Zr. Error

bars represent 1σ relative standard deviation on each analysis.